RESEARCH ARTICLE

Key Points:
- Observations and model simulations reveal perturbations in NOy partitioning up to 5 hPa, associated with moderate-magnitude volcanism
- Simulations indicate an aerosol-induced increase in ClO but at levels undetectable in available observations
- N₂O is a very effective tracer for removing circulation-related anomalies of trace gases in the stratosphere to identify volcanic chemistry

Supporting Information:
- Supporting Information S1

Correspondence to:
B. Zambri,
bzambri@mit.edu

Modeled and Observed Volcanic Aerosol Control on Stratospheric NO_y and Cl_y

Brian Zambri[1] iD, **Susan Solomon[1]** iD, **Douglas E. Kinnison[2]** iD, **Michael J. Mills[2]** iD, **Anja Schmidt[3,4]** iD, **Ryan R. Neely III[5,6]**, **Adam E. Bourassa[7]** iD, **Douglas A. Degenstein[7]**, and **Chris Z. Roth[7]**

[1]Department of Earth, Atmospheric, and Planetary Sciences, Massachusetts Institute of Technology, Cambridge, MA, USA, [2]Atmospheric Chemistry Observations and Modeling Laboratory, National Center for Atmospheric Research, Boulder, CO, USA, [3]Department of Chemistry, University of Cambridge, Cambridge, UK, [4]Department of Geography, University of Cambridge, Cambridge, UK, [5]National Centre for Atmospheric Science, University of Leeds, Leeds, UK, [6]School of Earth and Environment, University of Leeds, Leeds, UK, [7]Institute of Space and Atmospheric Studies, University of Saskatchewan, Saskatoon, Saskatchewan, Canada

Abstract Decreases in stratospheric NO_x associated with enhanced aerosol have been observed after large volcanic eruptions, for example, after the eruption of Mount Pinatubo in 1991. While the 1991 Mount Pinatubo eruption was the last large explosive eruption, recent studies have shed light on the impacts of moderate-sized eruptions since the year 2000 on the global stratospheric aerosol budget. We use an ensemble of simulations from a coupled climate-chemistry model to quantify and analyze changes in NO and NO_2 (NO_x), N_2O_5, HNO_3, ClO, and $ClONO_2$ during periods of increased stratospheric volcanic aerosol concentrations since 2000. By using an ensemble approach, we are able to distinguish forced responses from internal variability. We also compare the model ensemble results to satellite measurements of these changes in atmospheric composition, including measurements from the Optical Spectrograph and Infrared Imaging Spectrometer on the Odin satellite and the Aura Microwave Limb Sounder. We find decreases in stratospheric NO_x concentrations up to 20 hPa, consistent with increases in stratospheric HNO_3 concentrations. The HNO_3 perturbations also extend higher, up to 5 hPa, associated with periods of increased volcanic aerosol concentrations in both model simulations and observations, though correlations with volcanic aerosol are considerably higher in the model simulations. The model simulates increases in ClO at altitudes and magnitudes similar to the NO_x reductions, but this response is below the detectable limit in the available observations (100 pptv). We also demonstrate the value of accounting for transport-related anomalies of atmospheric trace gases by regression onto N_2O anomalies.

1. Introduction

Heterogeneous chemistry on the surfaces of sulfate aerosol injected by volcanic eruptions can affect NO_y (e.g., NO_2, N_2O_5, and HNO_3) and Cl_y (e.g., Cl, ClO, $ClONO_2$, and HCl) partitioning in the stratosphere (e.g., Coffey, 1996; Hanson et al., 1994). After large sulfur injections from the El Chichón (1982) and Pinatubo (1991) eruptions, extensive research was carried out to identify and quantify these responses. Johnston et al. (1992) and Mills et al. (1993) found large NO_2 reductions over New Zealand and Colorado, respectively, after Pinatubo; Rinsland et al. (1994) found decreases in N_2O_5 and increases in HNO_3; on the basis of on-ground and stratospheric aircraft measurements, Coffey (1996) found decreases in NO and NO_2 (hereafter NO_x) and corresponding increases in HNO_3 column abundances after both eruptions; Mickley et al. (1997) found reductions in NO_x as high as 17 hPa after Pinatubo, and Avallone et al. (1993) found increases in ClO near 20–30°N after Pinatubo.

The heterogeneous reactions that are thought to control the NO_y/Cl_y response to sulfate aerosol are as follows (Hanson et al., 1994):

$$ClONO_2 + HCl \rightarrow HNO_3 + Cl_2 \qquad (R1)$$

$$HOCl + HCl \rightarrow H_2O + Cl_2 \qquad (R2)$$

$$N_2O_5 + H_2O \rightarrow 2HNO_3 \qquad (R3)$$

$$ClONO_2 + H_2O \rightarrow HOCl + HNO_3 \tag{R4}$$

$$BrONO_2 + H_2O \rightarrow HOBr + HNO_3 \tag{R5}$$

As such, the expected responses to an increase in volcanic aerosol concentrations include a decrease in NO, NO_2, and N_2O_5 mainly by reaction (R3) (N_2O_5 is a reservoir species for NO and NO_2, and therefore, hydrolysis of N_2O_5 depletes the reservoir) and a corresponding increase in HNO_3 by (R3), as well as (R1), (R4), and (R5). Similarly, anomalies of opposite signs are possible in $ClONO_2$ (negative; (R1) and (R4)) and ClO (positive; (R1) and (R2)), though (R4) is likely most significant inside the polar vortex (Wegner et al., 2012).

There has been no eruption nearly as large in magnitude as Mount Pinatubo (18 Tg SO_2) since it erupted in 1991; however, on average about 0.8 Tg SO_2/year was emitted into the stratosphere from volcanic eruptions over 2005–2013, with injections as high as 21 km (Table S1 in the supporting information). This constitutes a substantial increase from the 0.06 Tg SO_2/year emitted, on average, over 1999–2004, and there has been an increasing focus recently on understanding the role of these smaller but still significant injections of volcanic sulfur into the stratosphere on, for example, the global energy budget and climate change (Schmidt et al., 2018; Solomon et al., 2011) and atmospheric chemistry (Adams et al., 2017; Berthet et al., 2017). For the latter, Berthet et al. (2017) found reductions of NO_2 and increased HNO_3 below 19 km after the 2009 Sarychev Peak eruption, while Adams et al. (2017) showed NO_2 reductions up to 25 km after several eruptions from 2005 to 2014, as measured by the Optical Spectrograph and Infrared Imaging System (OSIRIS).

Though the research on the topic is extensive, previous studies largely looked at the lowermost stratosphere, and only a few have examined the impacts of volcanic eruptions since 2000. The goal of this study is to probe not only the lower but also the upper layers of the stratosphere to investigate whether there are any significant observable responses in NO_y or Cl_y to the multiple moderate-magnitude volcanic eruptions in the post-Pinatubo era. Using satellite data from OSIRIS and the Microwave Limb Sounder (MLS), and an ensemble of simulations from the Community Earth System Model version 1 with the Whole Atmosphere Community Climate Model component (CESM1[WACCM4]; Hurrell et al., 2013; Mills et al., 2016), we examine the effect of recent volcanic eruptions on stratospheric composition up to 5 hPa.

The model ensemble approach is a powerful approach for separating forced responses from natural or internal variability (e.g., Deser et al., 2014; Kay et al., 2015; Otto-Bliesner et al., 2016). This approach is especially important for elucidating the responses to forcings, such as volcanic eruptions, which can alter not only the mean state but also the internal variability (e.g., Bittner et al., 2016). While the ensemble approach has been shown to be an effective tool in dynamical studies, it has seen less application for chemistry. Here we show the importance of making use of statistical information from ensemble simulations to ensure appropriate identification of chemical phenomena, especially when comparing data and models.

We also demonstrate the value of accounting for transport-related anomalies of atmospheric trace gases by regressing onto N_2O anomalies. This method has seen limited application in prior studies (e.g., Rinsland et al., 2009; Stolarski et al., 2018), but this work suggests that it can provide an improved means of accounting for quasi-biennial oscillation (QBO) perturbations to chemically active species.

2. Data and Model Description

2.1. CESM1(WACCM)

CESM1 is a fully coupled climate model with atmosphere, ocean, land, and sea ice components (Hurrell et al., 2013). WACCM version 4 is the high-top atmospheric component of CESM1 that has a horizontal resolution of 1.9° latitude by 2.5° longitude; the free running version of WACCM used here has 66 vertical levels with a model top near 140 km in altitude (Garcia et al., 2017; Marsh et al., 2013; Solomon et al., 2015). The WACCM chemical scheme used in the study includes a representation of tropospheric, stratospheric, mesospheric, and lower thermospheric chemistry (Kinnison et al., 2007; Tilmes et al., 2016). The species included within this mechanism are contained within the O_x, NO_x, HO_x, ClO_x, and BrO_x chemical families, along with CH_4 and its degradation products. In addition, 20 primary nonmethane hydrocarbons and related oxygenated organic compounds are represented along with their surface emissions. There is a total of 183 different species, 341 gas phase reactions, 114 photolytic processes, and 17 heterogeneous reactions on aerosols (i.e., sulfate, nitric acid trihydrate, and water ice).

Using this model, a fully coupled ensemble of simulations is generated. The ensemble uses a free running atmosphere-ocean chemistry climate general circulation model whose 10 members are examined over the 1999–2014 period, allowing a better distinction between the forced response and internal variability, thereby allowing us to identify to what extent any volcanic signals should be expected in the observations. These simulations have a repeated cyclic 28-month QBO based on rocketsonde data (Matthes et al., 2010) and no solar cycle. Sulfate aerosol surface area densities (SAD) include volcanic and nonvolcanic sources and are specified based on calculations from Mills et al. (2016), which used volcanic SO_2 injections from Neely and Schmidt (2016) for the period spanning 1999–2014. The calculated aerosol properties were shown to compare well to lidar-based stratospheric aerosol extinction data (Mills et al., 2016) and the Coupled Model Intercomparison Project phase 6 stratospheric aerosol optical depth data set (Schmidt et al., 2018; Thomason et al., 2018). Ensemble members are branched from a single Chemistry-Climate Model Initiative (Eyring et al., 2013) REF-C2 simulation in 1995, and distinct ensemble members are generated by randomly perturbing the initial temperature fields by roundoff magnitude (order 10^{-14} K). The SAD calculations are based on simulations nudged using meteorological fields from the NASA Global Modeling and Assimilation Office Modern-Era Retrospective Analysis for Research and Applications (Rienecker et al., 2011), including stratospheric winds, so the transport of aerosols is not affected by the cyclic QBO used in these simulations. Greenhouse gas concentrations in the simulations evolve according to the Representative Concentration Pathway 6.0 (Fujino et al., 2006; Hijioka et al., 2008), and concentrations of ozone-depleting substances are prescribed according to the Chemistry-Climate Model Initiative (Eyring et al., 2013).

2.2. MLS

The Earth Observing System MLS on board the Aura satellite launched 15 July 2004 observes thermal emission through the Earth's atmospheric limb, which enables daily near-global (82°S to 82°N) measurements of temperature, pressure, and atmospheric gases from the troposphere to the mesosphere (Waters et al., 2006). The data used in this study are MLS v4.2 "Level 2" products generated from the calibrated microwave irradiance observations; improvements in the v4.2 data include better handling of cloudy regions (Livesey et al., 2017).

The standard MLS ClO product is taken from the 640-GHz retrievals. The vertical resolution of the v4.2 ClO is 3–4.5 km. Precision on individual profiles is ±0.1 ppbv over most of the stratosphere, increasing to ±0.3 ppbv at 147 and 1 hPa. The systematic uncertainty in the measurements ranges from ±0.02 to ±0.4 ppbv. There exists a latitude-dependent bias in the ClO profiles in the 68 to 147 hPa range, which is corrected by subtracting the bias estimates from individual measurements at these levels. V2.2 ClO measurements are validated in Santee et al. (2008); for a similar comparison of different observing platforms with v3 ClO products, to which the v4.2 ClO product is most similar, see Livesey et al. (2013).

For pressures greater than or equal to 22 hPa, the MLS HNO_3 product is derived from the 240-GHz radiances; for pressures less than 22 hPa, retrievals from the 190-GHz radiometer are used. The vertical resolution of the v4.2 HNO_3 is 3–5 km. Precision on individual profiles is ±0.6 ppbv over most of the stratosphere, increasing to ±0.8 and ±1.2 ppbv at 2.1 and 1.5 hPa, respectively, and systematic uncertainties are between ±0.1 and ±2.4 ppbv at the various levels (Livesey et al., 2017). The detailed validation of the v2.2 HNO_3 products is presented by Santee et al. (2007), with analysis of the more comparable v3 HNO_3 measurements in Livesey et al. (2013).

Previous versions of MLS N_2O were derived from the 640-GHz retrievals. However, due to deterioration of the derived N_2O product, the standard product for MLS v4.2 N_2O is taken from the 190-GHz radiances. The vertical resolution of the 190-GHz N_2O product is 4–8 km, and the estimated precision varies from ±15 to ±19 ppbv; these values are slightly worse than those of the 640-GHz retrievals, except at 68 hPa (Livesey et al., 2017). Compared to v2.2 N_2O, which is validated in Lambert et al. (2007), average v4.2 N_2O values are up to 10% smaller at 100 and 68 hPa and within a few percent at other levels.

After screening individual profiles as described in Livesey et al. (2017), MLS ClO, HNO_3, and N_2O retrievals are averaged to create daily means on 7.5° latitude × 15° longitude grids; daily means are then averaged zonally and in time to construct monthly zonal averages on each pressure level. Because the focus of this

analysis is partially on the effectiveness of the N_2O regression fit, analysis of MLS products is performed on the intersection of the N_2O and ClO/HNO_3 vertical grids: 68–1 hPa for ClO and 68–1.5 hPa for HNO_3.

2.3. OSIRIS

OSIRIS is a Canadian instrument on board the Swedish Odin satellite (Llewellyn et al., 2004; McLinden et al., 2012). Launched on 20 February 2001, the orbit of OSIRIS is Sun-synchronous, at an altitude of approximately 600 km. Similar to MLS retrievals, limb-scattering measurements from OSIRIS have near-global, 82°S to 82°N, spatial coverage. The OSIRIS data used in this study are based on the v6 NO_2, which are described and validated in Sioris et al. (2017). The v6 NO_2 data are based on an improvement of previously developed retrieval algorithms, and measurement uncertainties are estimated to be about 15–20% above ~20 km (Bourassa et al., 2011; Sioris et al., 2003, 2004, 2007).

Based on OSIRIS measurements during descending portions of the orbit, with an equatorial crossing time near 06:30 local solar time (LST), NO_2 number density profiles are derived. NO_2 (and NO) is in rapid photochemical equilibrium and exhibits a strong diurnal cycle (Brasseur & Solomon, 2005; Park et al., 2017, their Figure 1). In order to facilitate the comparison of the OSIRIS NO_2 observations with model output, Park et al. (2017) derived daily-mean NO_x (NO + NO_2) concentrations using a photochemical box model (Adams et al., 2017; McLinden et al., 2000; Prather, 1992). After adjusting the OSIRIS NO_2 profiles to represent NO_2 concentrations at 06:30 a.m. LST (some of the profiles are measured before or after 6:30 LST), the box model was used to derive a scaling factor based on the ratio of daily-mean NO_x concentrations to NO_2 concentrations at 6:30 LST; the scaling is then applied to estimate the daily average NO_x concentrations.

As in Park et al. (2017), we convert NO_x number densities to mixing ratios using temperature (T) and pressure (p) from the European Centre for Medium-Range Weather Forecasting (ECMWF) interim reanalysis (ERA-Interim; Dee et al., 2011). The box model includes input of OSIRIS O_3 and aerosol extinction, as well as the retrieved surface reflectance and T and p from ERA-Interim.

Gridded OSIRIS NO_x profiles are computed similarly to the MLS profiles: daily NO_x profiles are used to construct daily gridded data on the same horizontal grid as the MLS data, and the daily gridded data are averaged to create monthly zonal means. On the other hand, the OSIRIS NO_x product is available on a vertical grid of 1 km from 10.5 to 39.5 km, which we interpolate vertically to the MLS N_2O pressure grid using log-pressure coordinates.

3. Methods

We calculate the climatological monthly mean and standard deviation of the WACCM SAD, $\overline{SAD}$, and σ_{SAD}, respectively, at each latitude and pressure level for the period 1999–2013. We define the "volcanically active" periods at each latitude ϕ and pressure level p as the set of all times t such that

$$SAD(t,\phi,p) > \overline{SAD}(\phi,p) + \sigma_{SAD}(\phi,p) \tag{1}$$

In other words, we define a volcanically active period as one where the SAD is greater than one standard deviation above the mean for that month, latitude, and pressure level or approximately greater than the 84th percentile. The background climatologies, from which all anomalies are calculated, are then calculated as the means of the "volcanically clean" periods, that is, the times for which equation (1) is not satisfied. The background values are subtracted at all points, and the linear trend is removed. Finally, we divide by the background values, so that unless otherwise noted, anomalies are given as deseasonalized and detrended percent changes.

Figure 1 shows the deseasonalized and detrended WACCM NO_x anomalies for a single ensemble member (#5) at several levels in the stratosphere. Black contour lines in the figure highlight the periods of enhanced stratospheric aerosol concentrations as defined by equation (1), based upon the volcanic inputs and modal aerosol model presented in Mills et al. (2016). The figure suggests suppression of NO_x during periods of high aerosol concentrations at the lowest levels (72 and 51 hPa; Figures 1d and 1e) but with considerable noise. Overall, the most prominent feature is the 28-month periodic QBO signal, which can be seen at all levels in the tropics and midlatitudes in Figure 1. The effect of the QBO on stratospheric composition has been
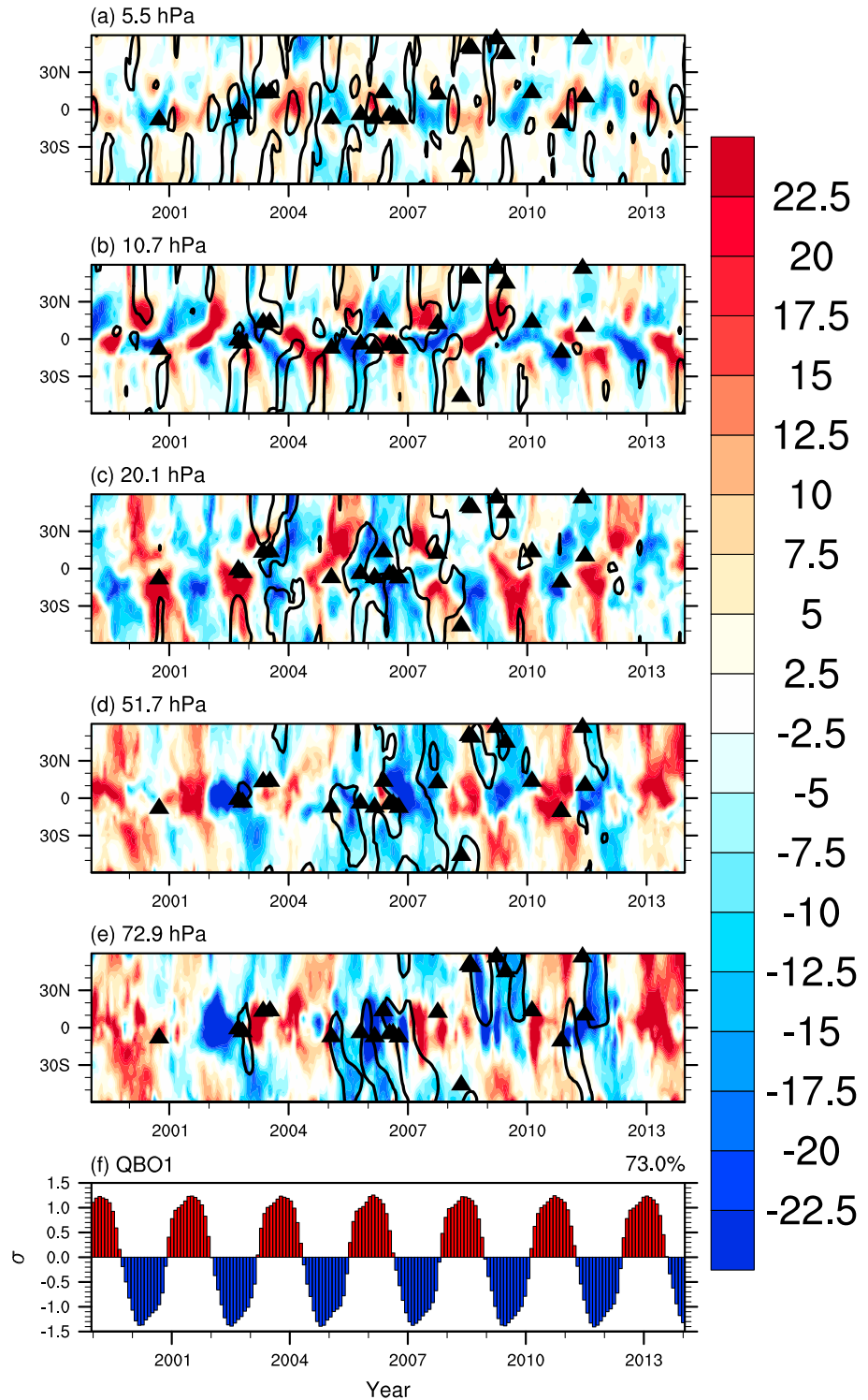
Figure 1. WACCM NO_x ($NO + NO_2$) anomalies (%; a–e) and QBO1 time series (f) for ensemble member 5. Black line contours indicate where sulfate aerosol surface area density is greater than 1σ above the mean, and triangles indicate the timing and latitudes of the volcanic eruptions listed in Table S1. The number in the top right corner of panel (f) is the percent variance of the zonal wind explained by QBO1. WACCM = Whole Atmosphere Community Climate Model; QBO = quasi-biennial oscillation.
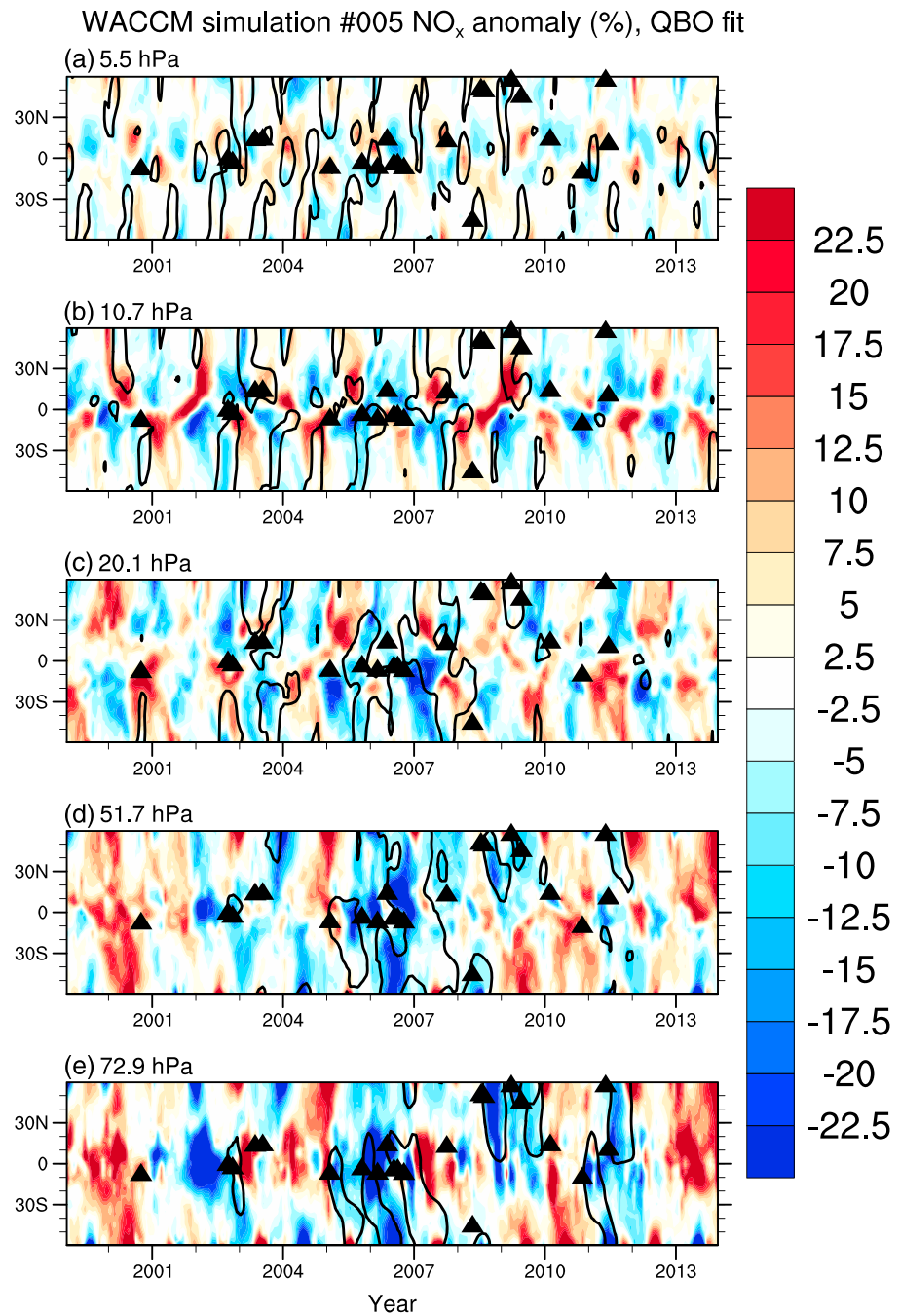
Figure 2. (a–f) WACCM NO_x anomalies (%) for ensemble member 5 with QBO1 + QBO2 fits removed. Black line contours indicate where sulfate aerosol surface area density is greater than 1σ above the mean, and triangles indicate the timing and latitudes of the volcanic eruptions listed in Table S1. WACCM = Whole Atmosphere Community Climate Model; QBO = quasi-biennial oscillation.

widely studied (e.g., Park et al., 2017; Randel & Thompson, 2011; Randel & Wu, 1996). We first present a fit to QBO-related anomalies obtained using a multiple linear regression, regressing the first two principal components (PCs) of the QBO (QBO1 and QBO2, respectively) onto the WACCM NO_x anomalies (Adams et al., 2017; Bourassa et al., 2014; Park et al., 2017; Randel & Wu, 1996); the results of the fit are plotted in Figure 2, and the relative amplitudes of the QBO regression fits are given in Figures 3a and 3b. After regressing out the first two PCs of QBO, altitudes above 50 hPa still show a clear quasi-biennial signal on WACCM NO_x anomalies (period ~22 months; Figures 2a–2c). We chose to show WACCM NO_x anomalies
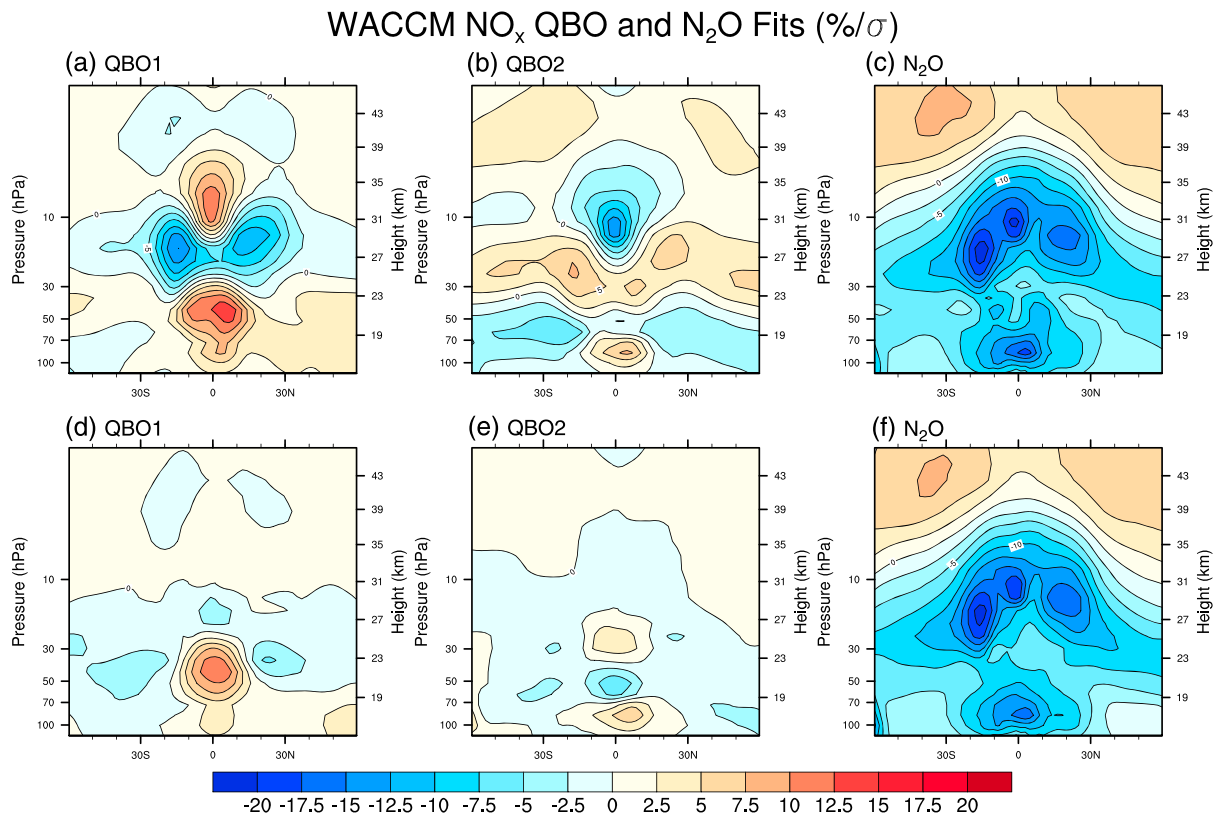
Figure 3. Relative amplitude of regression fits (%/σ) for WACCM NO_x for QBO only (a, b), N_2O only (c), and QBO + N_2O (d–f). Results are shown for the mean of the regression fits of the individual ensemble members. WACCM = Whole Atmosphere Community Climate Model; QBO = quasi-biennial oscillation.

as an illustrative example here, but this pattern is consistent across the different gases analyzed (and between model and observations). We also investigated the impacts of the semiannual oscillation (SAO) of zonal winds in the tropical upper stratosphere but found little correlation between the SAO and NO_y concentrations, so SAO regression is excluded from results shown here. Instead, the residual quasi-biennial signal at upper levels appears to be a tape recorder-like effect (Mote et al., 1996), where QBO-induced anomalies at lower levels are advected upward, with variable time lags relative to lower levels.

Park et al. (2017) demonstrated the strong anticorrelation between NO_x and HNO_3 and source gas N_2O in the tropical stratosphere, where N_2O is oxidized to form NO_y. We next explore this relationship and its value for accounting for dynamical variability including the QBO. In Figure 4, scatter plots of deseasonalized and detrended N_2O versus NO_y ($NO + NO_2 + NO_3 + 2N_2O_5 + HNO_3 + ClONO_2$) anomalies at various levels and latitude bands demonstrate this relationship, which extends outside the tropical latitudes studied by Park et al. (2017). At all pressure levels above and including 72 hPa (i.e., at pressures less than or equal to 72 hPa), NO_y shows strong anticorrelations with N_2O, except at high latitudes in the upper stratosphere (poleward of 30° in both hemispheres at 5 hPa; Figure 4a), where NO_y is positively correlated with N_2O, with Pearson correlation coefficients greater than 0.5. Correlation coefficients between N_2O and NO_y are below −0.9 at all levels in the 10°S to 10°N band, with the strongest anticorellation ~−0.99 at 5 and 10 hPa (Figures 4a and 4b). At and below 20 hPa (Figures 4c–4e), correlation coefficients are below (i.e., stronger than) −0.9 at all latitudes in the 60°S to 60°N band considered here.

Park et al. (2017) showed the dependence of N_2O on the QBO; therefore, regressing N_2O anomalies onto the NO_y anomalies should also capture QBO variability. Because of the compact relationship between NO_y species and N_2O seen in Figure 4, this method should better account for sources of dynamical variability that regressing out QBO alone might not capture. In Figure 5, we show the WACCM NO_x time series obtained when detrended model N_2O anomalies are regressed onto the NO_x anomalies instead of using the QBO PCs; the relative amplitude of the N_2O fit is shown in Figure 3c. The tight relationship between N_2O and
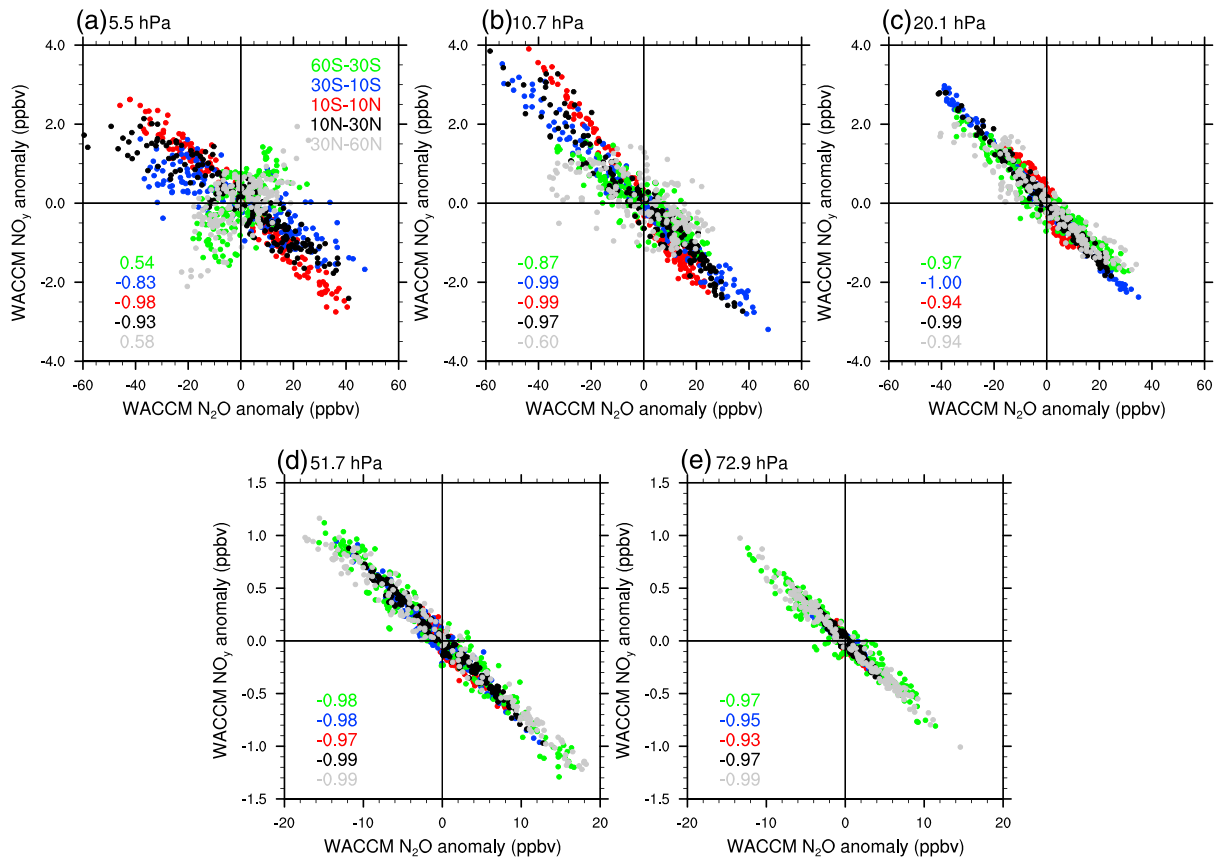
Figure 4. (a–e) Scatter plots of detrended WACCM NO_y ($NO + NO_2 + NO_3 + 2N_2O_5 + HNO_3 + ClONO_2$) versus N_2O anomalies. Pearson correlation coefficients for each latitude band (key at top right of panel a) are displayed at bottom left of each panel. Results shown are for ensemble member 5. WACCM = Whole Atmosphere Community Climate Model.

NO_y is further demonstrated in Figure 3c, which shows up to 20% decreases in NO_x for a 1σ change in N_2O in the tropical middle stratosphere (e.g., near 0° and 10 hPa). At levels above 50 hPa (Figures 5a–5c), the periodic oscillations are now well removed by regressing out N_2O anomalies, and novel information is obtained about the relationship between aerosol anomalies and NO_x. Specifically, at 10 and 20 hPa notable decreases in NO_x concentrations exceeding 10% are simulated in times of increased volcanic aerosol (Figures 5b and 5c). On the other hand, upon comparison of Figures 2d and 5d, there is now a QBO signal at 51 hPa (Figure 5d) which was not evident after removing the dynamical influence associated with QBO1 and QBO2 (Figure 2d). This is likely to be related in part to weak gradients in N_2O at lower altitudes (higher pressures). In light of the effectiveness of the N_2O regression above 50 hPa and the apparent utility of the QBO regression at greater pressures, we next use a multiple linear regression to remove dynamical anomalies associated with both the QBO and N_2O; the results are shown in Figure S1, and Figure 3 shows the relative amplitudes of the regression fits for each of the three methods ([a–b] QBO, [c] N_2O, and [d–f] QBO + N_2O). Figure 3 demonstrates that the N_2O anomalies dominate the QBO + N_2O regression; this should be expected, since N_2O anomalies will capture some of the QBO variability. However, Figures 3d and 3e show that retaining the QBO fit as a separate function remains important for optimal fitting at pressures ≥30 hPa. We note that the QBO also impacts the temperature structure of the stratosphere, which affects temperature-dependent chemistry; Figure S1 shows that using both the QBO and N_2O anomalies in the regression provides a remarkably effective means for accounting for both chemical and dynamical influences on NO_y, demonstrating the value of this approach for studies of chemical perturbations. Figure S2 shows the relative regression amplitudes for N_2O and the QBO. Stratospheric N_2O is highly correlated with the QBO above 30 hPa; on the other hand, variability in the equatorial stratospheric zonal winds has little influence on N_2O concentrations at and below 30 hPa. In
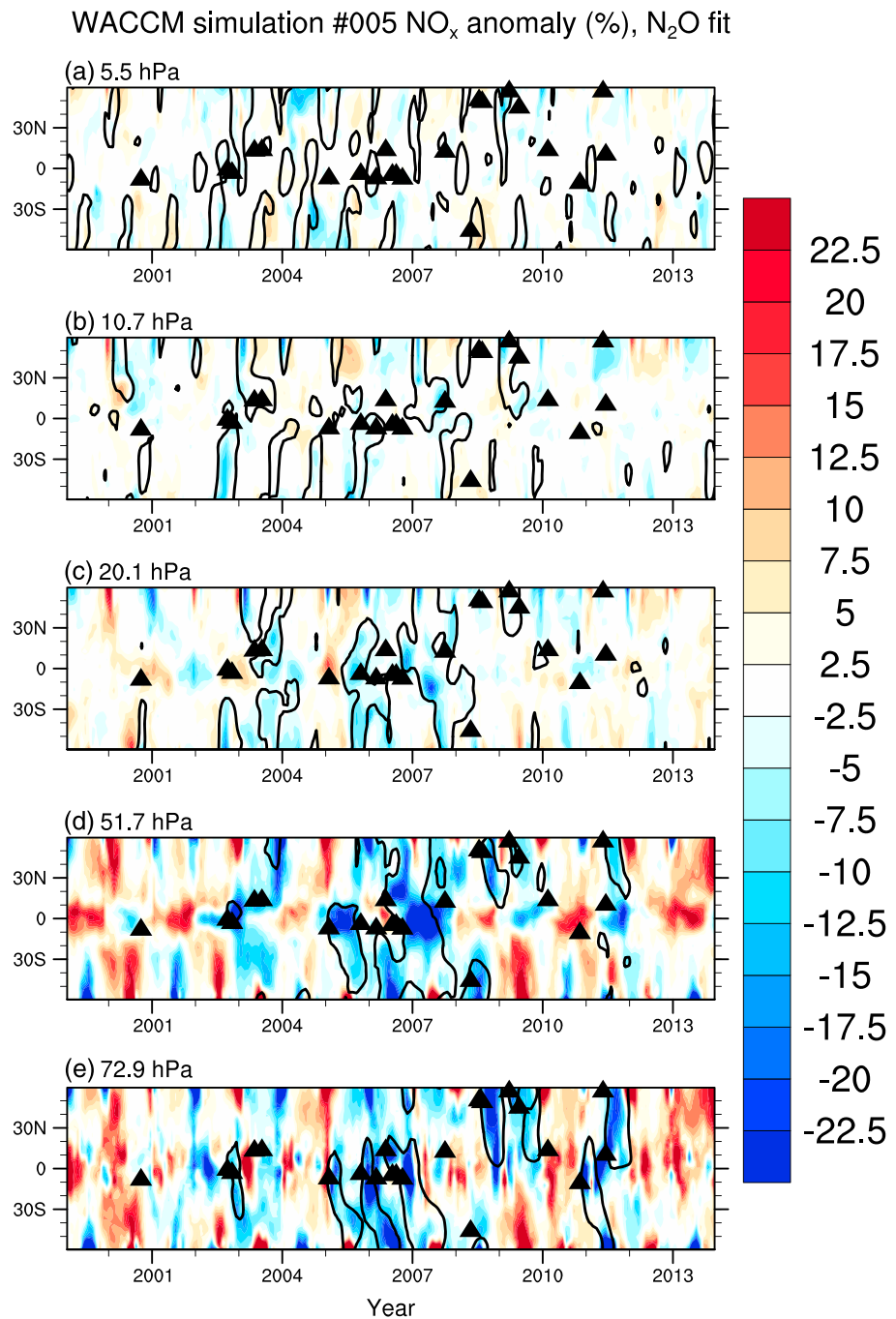
Figure 5. (a–e) WACCM NO_x anomalies (%) for ensemble member 5 with the dynamical variability identified by the N_2O fit removed. Black line contours indicate where sulfate aerosol surface area density is greater than 1σ above the mean, and triangles indicate the timing and latitudes of the volcanic eruptions listed in Table S1. WACCM = Whole Atmosphere Community Climate Model.

addition, Figure S3 shows the WACCM ensemble-mean NOx anomalies subtracted from those after N_2O regression only, which is approximately equal to the effect of including the QBO regression. From Figure S3, it can be concluded that the QBO influence for the QBO+N2O fit is limited to exactly those levels (pressure $\geq$ 30 hPa) where QBO and N_2O are uncorrelated. Therefore, the potential nonorthogonality of the QBO and N_2O regressors is not an issue for this application.

We also make use of the ensemble of coupled climate-chemistry model simulations by analyzing the signal-to-noise ratio (SNR; e.g., Deser et al., 2014). We define the SNR as the ensemble-mean anomaly—the "forced" response—divided by the standard deviation of the response across ensemble members, which quantifies the internal variability. The SNR analysis provides a quantitative comparison of the respective magnitudes of the forced response and the internal variability; this is useful for comparing the model ensemble to the observations in that it can help to identify times and locations in the observations at which one might best be able to see a forced response that is distinguishable from the natural variability.

4. Results

After removing the dynamics-related anomalies, there is a clear volcanic signal in the WACCM ensemble mean NO_x time series in Figure 6, with anomalies related to increased sulfate aerosol concentrations (contours show SAD) at levels up to 10 hPa but most prevalent at and below 20 hPa (i.e., at pressures $\geq$20 hPa). Specifically, at 10 hPa (Figure 6b), decreased NO_x concentrations are simulated poleward of 30°S in 2002–2004 during periods of increased volcanic aerosol concentrations; however, the timing of the response in 2002, which begins in July, indicates that the reduction is not related to the Ruang eruption, which occurred in September 2002. Reductions in NO_x are also simulated at NH midlatitudes in 2003, 2007, and 2008 in association with higher volcanic aerosol concentrations. The times and locations of these responses are consistent with volcanic aerosol concentration increases due to the eruptions listed in Table S1. The SNR in Figure 8b indicates that the most consistent forced anomaly at 10 hPa occurs in the NH tropics in 2007, where the SNR is above 4, indicating robustness of the reduction. In addition, Figure S4, which shows the absolute NO_x anomalies, indicates that the apparent correlation between aerosol concentrations and NO_x prior to 2005 is less robust, with both positive and negative anomalies simulated in times of increased aerosol concentrations. It is likely that the previously discussed reductions at midlatitudes in Figure 6b are partly related to the apparent seasonal cycle of sulfate aerosol SAD at this altitude. However, removal of the seasonal variations in the gaseous species demonstrates a robust aerosol chemical effect: comparing, for example, years 2002–2005, where this seasonal cycle is apparent, to 2010–2014, when the aerosol SAD is reduced at this level, it can be seen that these reductions in NO_x, though occurring seasonally, also vanish when the SAD is reduced.

Panels c–e in Figures 6 and 7 show reductions in NO_x that are both greater in magnitude and more directly related to identifiable volcanic injections. At 20 hPa (Figure 6c), similar decreases related to the seasonal occurrence of increased volcanic aerosol concentrations are simulated robustly in 2002 (SH) and 2003 (NH). On the other hand, NO_x reductions in the second half of 2003 and early 2004 are simulated from 30°N and southward and appear to be related to the 2003 Anatahan and/or Soufrière Hills eruptions (Table S1, based on Table S6 of Mills et al., 2016; eruption latitudes 16°N and 17°N, respectively). Again, the reductions there are less than 10%, but the SNR (Figure 8c) is above 4, indicating a chemical response to the increased volcanic aerosol concentrations that is robust and consistent across the model ensemble and therefore should be detectable in the single realization available in observations. The largest NO_x reductions at 20 hPa are simulated in 2005 (Manam, 4°S, Sierra Negra, 1°S; reductions >10%) and 2006 (Manam, 4°S, Soufriere Hills, 17°N, Tungurahua, 1°S; reductions >15%), with both periods simulating SNR above 4 (Figure 8c), again indicating that the signal should be observable. At 51 and 72 hPa (panels d and e of Figures 7 and 8), the volcanic aerosol effect is much more apparent, with WACCM model ensemble mean NO_x decreases of more than 20% in the tropics after Manam (4°S) and Sierra Negra (1°S; 2005); after Manam (4°S), Soufrière Hills (17°N), and Rabaul (4°S; 2006), with decreases lasting through 2007; and after Merapi (15°N) and Nabro (13°N; 2010–2011). Outside the tropics, large decreases are simulated in the SH after Manam (4°S, 2006), Rabaul (4°S; 2006; NO_x reduction in 2007), Chaitén (43°S; 2008), and Merapi (8°S; 2010; NO_x reduction in 2011). At NH midlatitudes, the largest reductions follow the eruptions of Soufriere Hills (17°N; 2006), Okmok (53°N), Kasatochi (52°N; 2008), Redoubt (60°N), Sarychev Peak (48°N; 2009), and Nabro (13°N; 2011). Figure S4 shows the absolute changes in NO_x in parts per billion by volume (ppbv), which are consistent with the percent changes in that the largest decreases are associated with increased volcanic aerosol, especially at and below 20 hPa. N_2O_5 anomalies (Figure S5) show similar decreases in response to the volcanic aerosol, with decreases exceeding 25% at ~50 hPa and below (Figures S5d–S5e).
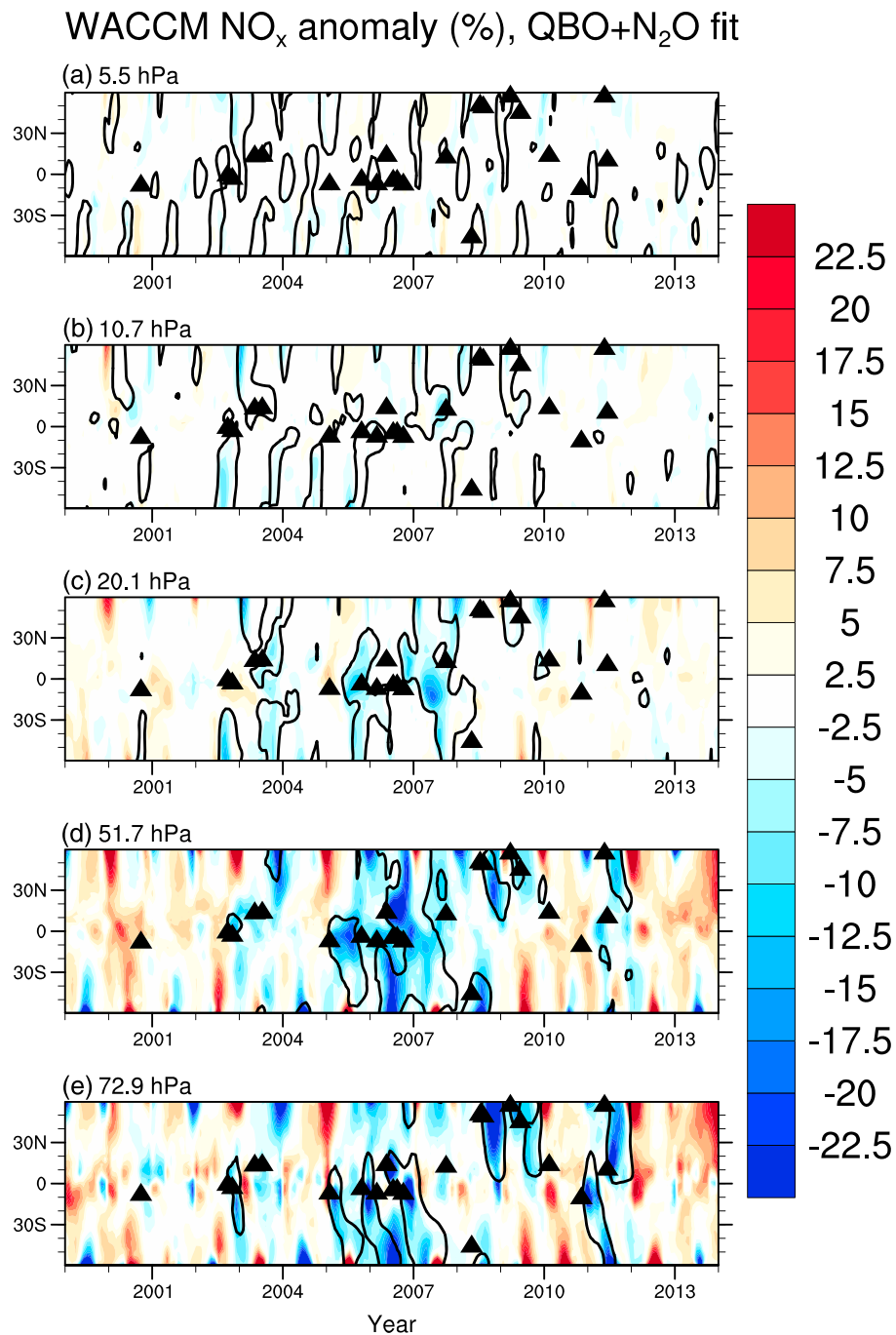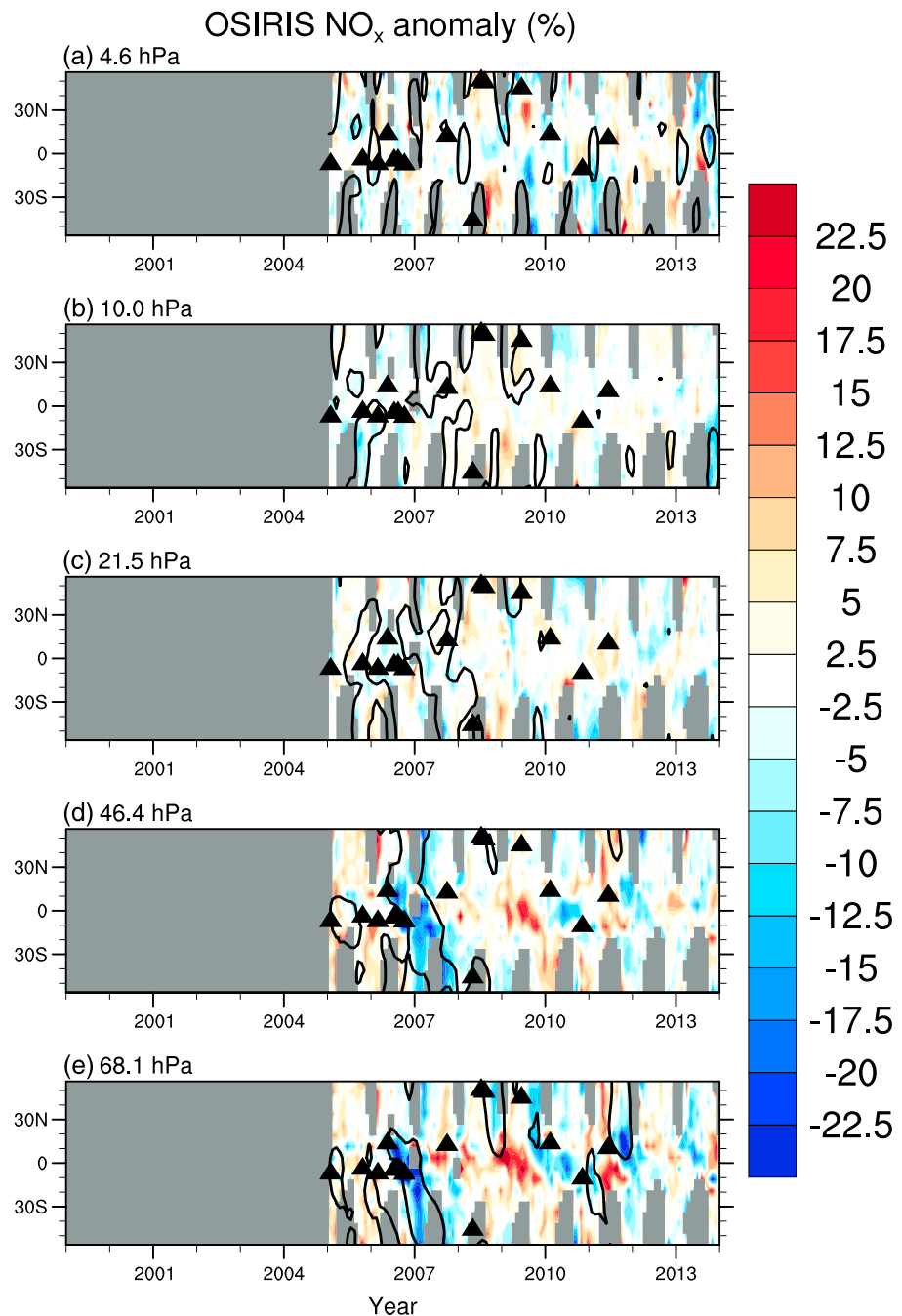
Figure 6. (a–e) WACCM NO_x anomalies (%) for the ensemble mean with QBO + N_2O fits removed. Black line contours indicate where sulfate aerosol surface area density is greater than 1σ above the mean, and triangles indicate the timing and latitudes of the volcanic eruptions listed in Table S1. WACCM = Whole Atmosphere Community Climate Model; QBO = quasi-biennial oscillation.

To further emphasize the added value of using N_2O as a tracer to remove anomalies related to dynamics, the WACCM NO_x SNR are shown after regressing out QBO only (Figure S6) and N_2O only (Figure S7). Comparison of SNR after QBO fit (Figure S6) with SNR after QBO + N_2O fit (Figure 7) shows that the full fitting process is much more effective in isolating the volcanic signal from dynamical variability. When using the QBO-only approach, Figure S6 shows SNR frequently above 4 at all levels, with the same spatiotemporal patterns as the residual periodic oscillations seen in Figure 2. The high SNR and therefore low variability
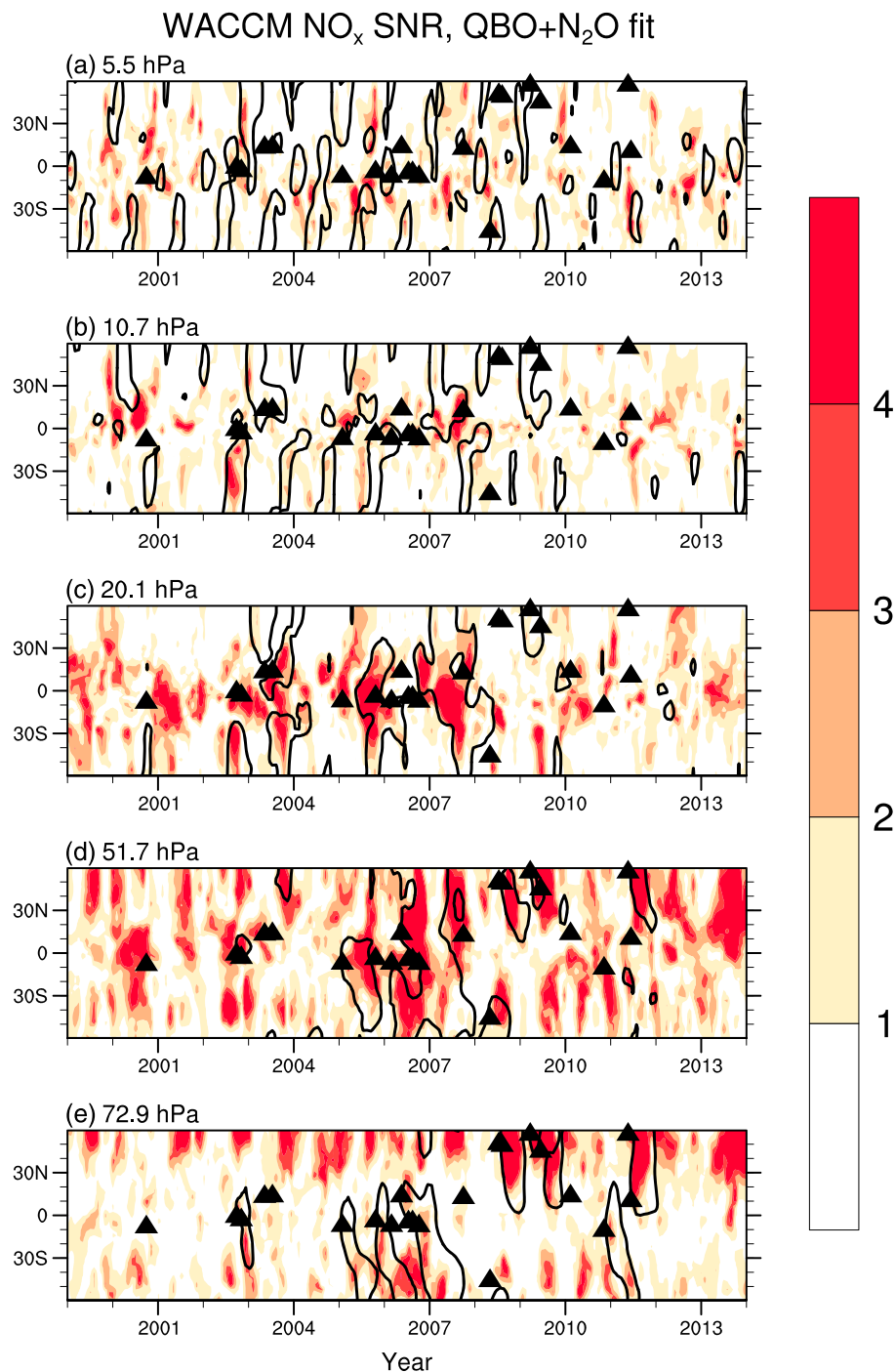
Figure 7. (a–e) WACCM NO_x signal-to-noise ratio (SNR), defined as the ensemble mean divided by the standard deviation across ensemble members. Black line contours indicate where sulfate aerosol surface area density is greater than 1σ above the mean, and triangles indicate the timing and latitudes of the volcanic eruptions listed in Table S1. WACCM = Whole Atmosphere Community Climate Model; QBO = quasi-biennial oscillation.

indicates a continued dynamical control on the simulated response, even after regression of the QBO influence. In contrast, Figure 7 shows that after the more robust removal of dynamics-related anomalies, SNR is either generally very low (e.g., Figures 7a and 7b) or that the high SNR is associated with increases in volcanic aerosol concentrations (Figures 7c–7e). A similar comparison between Figure 7 and S7 shows that the N_2O fit appears to be sufficient at higher altitudes but does not account for all dynamical

Figure 8. (a–e) OSIRIS-derived NO_x anomalies (%) with QBO + N_2O fits removed. Black line contours indicate where sulfate aerosol surface area density is greater than 1σ above the mean, and triangles indicate the timing and latitudes of the volcanic eruptions listed in Table S1. OSIRIS = Optical Spectrograph and Infrared Imaging System.

variability below 20 hPa, where high SNR remain, unrelated to volcanic aerosol concentrations (Figures S7c–S7d).

Figure 8 shows the OSIRIS NO_x observed anomalies in percent change, and absolute anomalies (ppbv) are given in Figure S8. For all observations (i.e., OSIRIS NO_x and MLS HNO_3 and ClO), we perform the same regression fit as was done for the model output, using MLS N_2O for the N_2O regression and using the equatorial zonal wind observations over Singapore (Naujokat, 1986) to compute the QBO components. The WACCM ensemble mean shows good agreement with the OSIRIS NO_x time series in Figure 8, with both

showing the largest reductions at 46 and 68 hPa, though the observations match better when compared with a single ensemble member, for example, Figure S1. Comparing the observations to a single ensemble member results in generally better agreement because much of the internal variability is averaged out when computing the ensemble mean response. In comparing WACCM simulation #5 (Figure S1) with the OSIRIS data (Figure 8), the two show very good agreement at all latitudes from July 2006 to 2008, with long-lasting reductions in NO_x in response to the sustained increase in volcanic aerosol during these years. In addition, the responses to Okmok (53°N) and Kasatochi (52°N; 2008), Sarychev Peak (48°N; 2009), Merapi (8°N; 2010), and Nabro (13°N; 2011) as seen in WACCM are also captured in the OSIRIS observations. On the other hand, a few key differences can also be seen. First, at 46 and 68 hPa, there is no observable reduction due to the increased volcanic aerosol concentrations after the Manam (4°S) eruption in 2005; this is consistent with Adams et al. (2017), who also showed minimal observed changes in response to this eruption. For the eruptions after 2008, the response in OSIRIS NO_x appears only at 68 hPa, as opposed to the WACCM simulations, which show reductions at 50 hPa in 2008, 2009, and 2011; this suggests potential differences between the observed and modeled transport of aerosol to the higher altitudes. The response to Okmok (53°N) and Kasatochi (52°N; 2008) is much larger and has greater latitudinal extent in the WACCM simulations than in the OSIRIS data.

WACCM ensemble mean HNO_3 anomalies (%) were analyzed in the same manner as those for NO_x presented above and are plotted in Figure 9. In contrast to NO_x, which shows the largest effect of aerosol below 20 hPa, Figure 9 shows that WACCM simulates impacts on HNO_3 throughout the stratosphere, with large percentage increases at 5 hPa during times of increased sulfate aerosol (Figure 9a). At 10 hPa (Figure 9b), WACCM simulates increases in HNO_3 following Manam (4°S; 2005 and 2006), Soufriere Hills (17°N), Rabaul (4°S; 2006; HNO_3 response in 2007), Okmok (53°N), and Kasatochi (52°N; 2008; HNO_3 response in 2009). At 20 and 72 hPa (Figures 9c and 9e), the aerosol-induced increases in HNO_3 are similar in magnitude to the associated decreases in NO_x (e.g., Figures 6c and 6e); at 51 hPa (Figure 9d), percent changes in HNO_3 are lower than those for NO_x (Figure 6d) and mostly confined to the tropics. WACCM HNO_3 SNR analysis (Figure S9) is consistent with Figure 9, although SNR at volcanically active times is hard to distinguish from the background SNR at 5 hPa (Figure S9a). The responses in Figure 9 at 10–72 hPa appear to be robust, as SNR at these altitudes tends to be highest during times of increased volcanic aerosol concentrations (Figures S9b–S9e). The model results compare well to HNO_3 observations from MLS (Figure 10), which show increases at times of increased volcanic aerosol concentrations at all levels but 46 hPa. Figures S10 and S11 show the absolute changes in HNO_3 for WACCM and MLS, respectively; the time series in these two figures agree quite well at all levels except near 50 hPa, where any concurrence of increased volcanic aerosol concentrations and MLS HNO_3 appears to be spurious.

WACCM ensemble mean ClO anomalies are plotted in Figure 11. Because of its presence at very low mixing ratios in the stratosphere, we present ClO anomalies as absolute anomalies in parts per trillion by volume (pptv). WACCM simulates increases in ClO at 10 hPa and below, with anomalies of similar magnitudes to the WACCM NO_x reductions. SNR analysis for the ClO response (Figure S12) indicates that the anomalies at 10 hPa, though consistent in terms of their coincidence with increased volcanic aerosol concentrations, may be difficult to distinguish from natural variability in the observations. The most distinct volcanic responses, as determined by high SNR relative to the background periods, are at 51 hPa in 2006–2007 and at 51 and 72 hPa in 2008, 2009, and 2011. WACCM $ClONO_2$ anomalies (Figure S13) show no discernible response to the increased volcanic aerosol, which indicates that the ClO increase at these levels is simply a result of the reductions in NO_2 and not related to chlorine heterogeneous chemistry (e.g., (R1) and (R4)).

MLS ClO show consistent increases associated with volcanic aerosol at 4 hPa only (Figure S14a), which is the opposite of the vertical extent of the response simulated in WACCM. Anomalies at 21 hPa are generally positive at times of increased volcanic aerosol concentrations as well, specifically in 2007, at NH midlatitudes in 2009 and in the tropics in 2011 after Nabro (13°N; though this does not meet the 1σ aerosol criterion). However, anomalies in 2005 at the same level do not appear to be affected by increased volcanic aerosol concentrations. Overall, positive MLS ClO anomalies at times of increased volcanic aerosol concentrations do not stand out when compared to anomalies during volcanically clean periods. However, the changes in ClO simulated by WACCM are well below 100 pptv, which is the reported precision of the MLS product at these levels; therefore, it is probably the case that this response is simply undetectable in the observations.
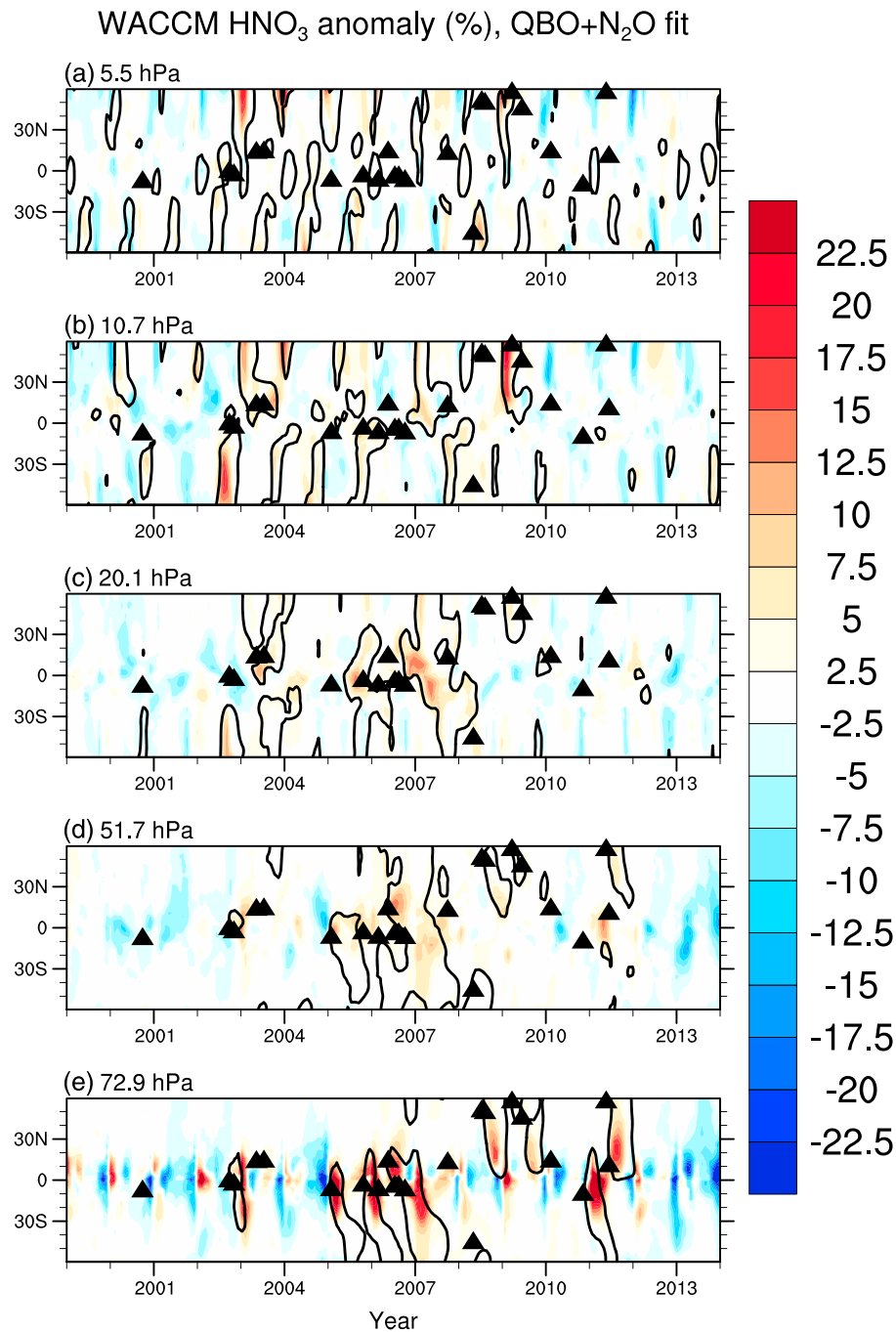
Figure 9. (a–e) WACCM HNO_3 anomalies (%) for the ensemble mean with QBO + N_2O fits removed. Black line contours indicate where sulfate aerosol surface area density is greater than 1σ above the mean, and triangles indicate the timing and latitudes of the volcanic eruptions listed in Table S1. WACCM = Whole Atmosphere Community Climate Model; QBO = quasi-biennial oscillation.

5. Discussion

Figure 12 shows the Pearson correlation coefficients between sulfate aerosol SAD and the simulated and observed changes in NO_x, HNO_3, and ClO. For WACCM (Figures 12a–12c), the mean of the correlations from the ensemble members is shown; the correlations from individual ensemble members are in general very similar. WACCM simulates high anticorrelations between NO_x and SAD (Figure 12a), with correlation coefficients less than −0.8 in the 20°S to 20°N band and from about 50–20 hPa. High
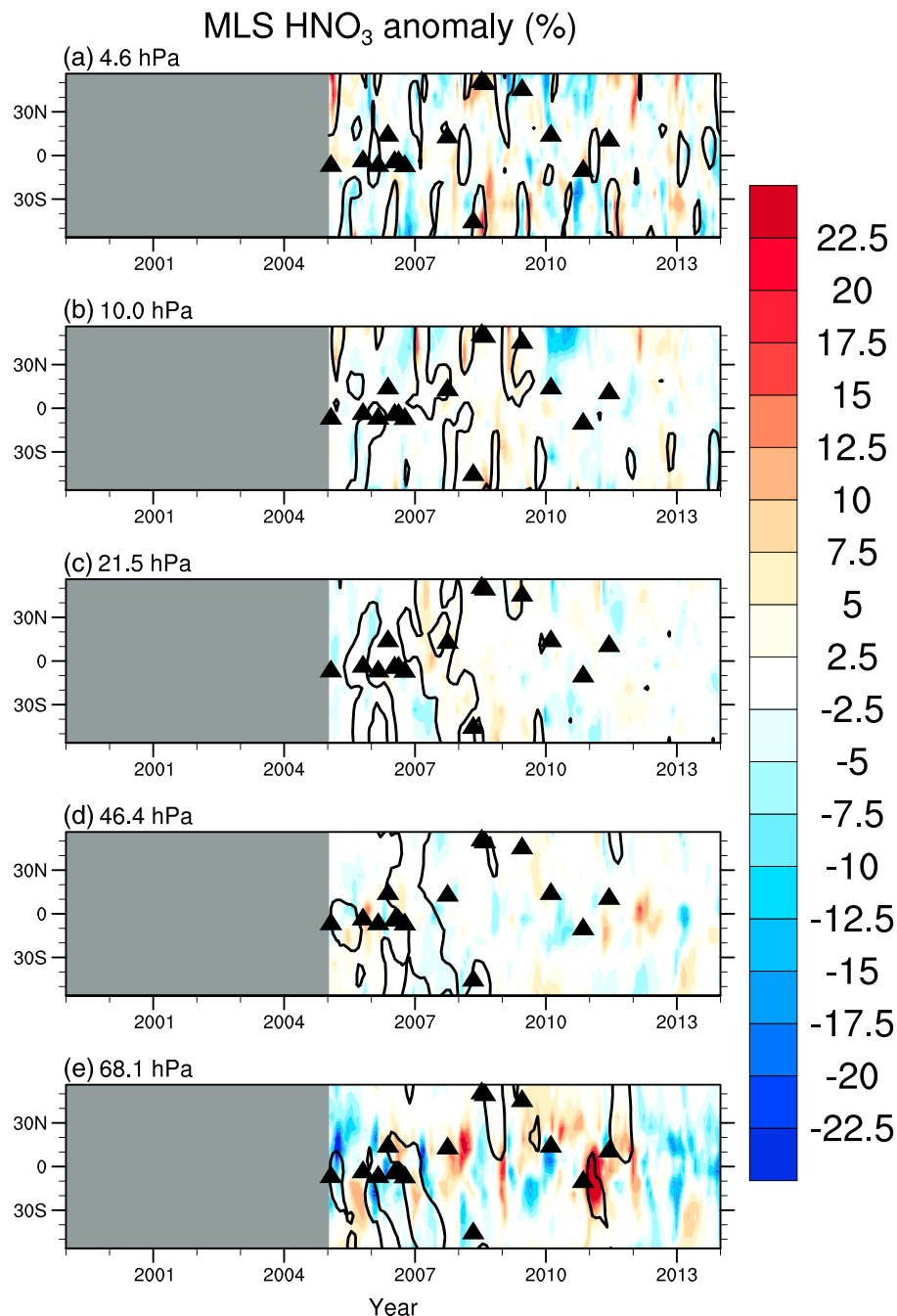
Figure 10. (a–e) MLS HNO_3 anomalies (%) with quasi-biennial oscillation + N_2O fits removed. Black line contours indicate where sulfate aerosol surface area density is greater than 1σ above the mean, and triangles indicate the timing and latitudes of the volcanic eruptions listed in Table S1. MLS = Microwave Limb Sounder.

correlations between HNO_3 and SAD (Figure 12b) are also simulated in WACCM, with correlations as high as 0.5 extending upward past 10 hPa, in agreement with the WACCM HNO_3 time series discussed above. ClO correlations with SAD (Figure 12c) show a similar spatial pattern to the NO_x correlations but are generally lower in magnitude. In all three species, the magnitudes of the correlations generally decrease with increased distance from the equator. It is likely that higher aerosol concentrations and longer aerosol lifetimes in the tropics contribute to the generally higher correlations at these latitudes.

Figure 11. (a–e) WACCM ClO anomalies (pptv) for the ensemble mean with QBO + N_2O fits removed. Black line contours indicate where sulfate aerosol surface area density is greater than 1σ above the mean, and triangles indicate the timing and latitudes of the volcanic eruptions listed in Table S1. WACCM = Whole Atmosphere Community Climate Model; QBO = quasi-biennial oscillation.
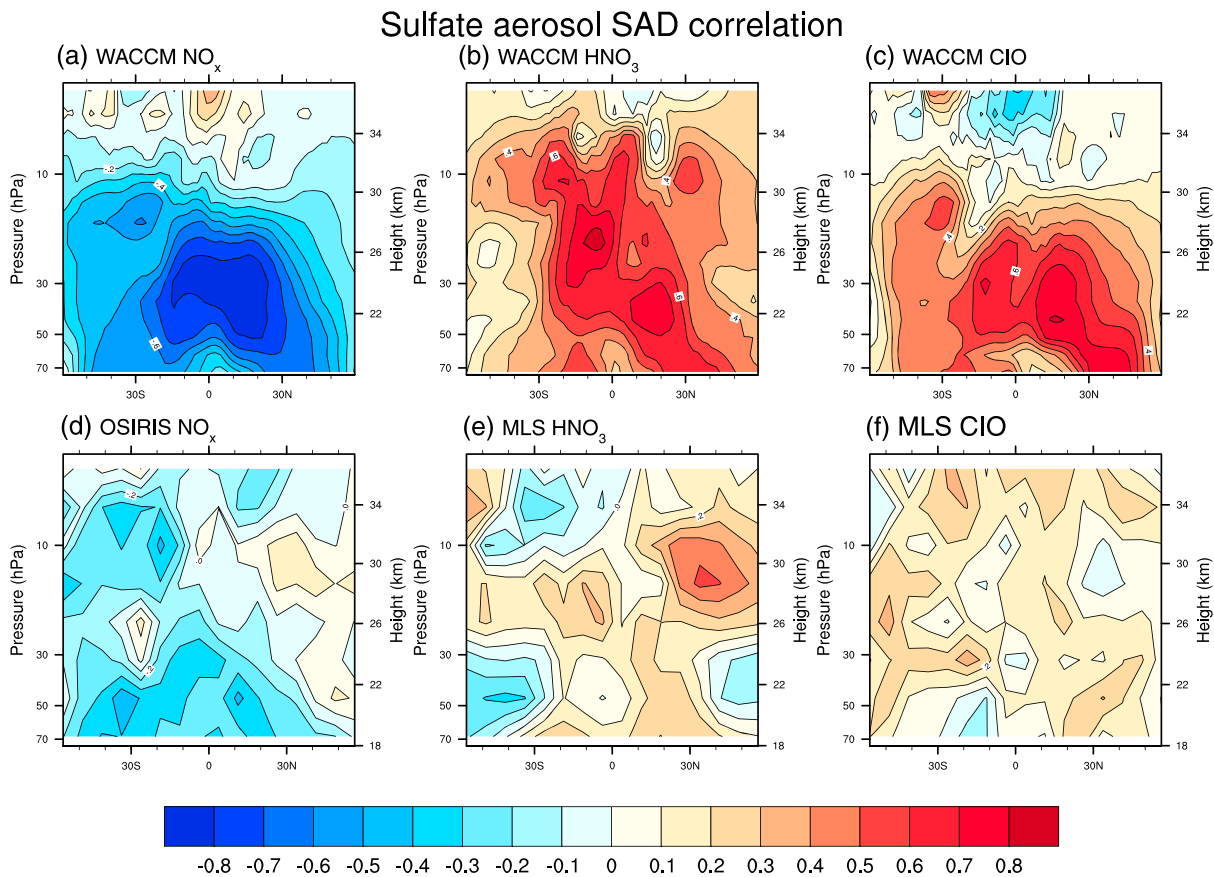
Observations in Figures 12d–12f show overall good agreement on the sign of the correlation, and the top and bottom rows appear to be spatially coherent, with Pearson correlation coefficients of 0.57, 0.56, and 0.28 below 10 hPa for NO_x, HNO_3, and ClO, respectively. On the other hand, the magnitudes of the observed correlations are generally much lower than those simulated in WACCM. In addition, there are several noticeable differences in Figure 12 between the model (top row) and observations (bottom row). OSIRIS NO_x-

Figure 12. Pearson correlation coefficients of sulfate aerosol surface area density and (a) WACCM NO_x, (b) WACCM HNO_3, (c) WACCM ClO, (d) OSIRIS NO_x, (e) MLS HNO_3, and (f) MLS ClO. WACCM results shown are the mean of the correlation coefficients of the individual ensemble members. WACCM = Whole Atmosphere Community Climate Model; OSIRIS = Optical Spectrograph and Infrared Imaging System; MLS = Microwave Limb Sounder.

aerosol correlations (Figure 12d) appear to be the lowest in the 20-hPa range and are actually larger than WACCM correlations (Figure 12a) at 10 hPa and above. The spatial patterns of HNO_3-aerosol correlations agree quite well between WACCM and MLS at and below 10 hPa (Figures 12b and 12e, respectively) and at 5 hPa in the NH. Correlations between MLS ClO and volcanic aerosol are mostly positive (Figure 12f), in agreement with the WACCM simulations (Figure 12c), though as previously mentioned, Figure S14 indicates that these correlations are purely coincidental.

Though the chemical response to volcanic aerosol was identified robustly in both the model and the observations, we have also identified at some points considerable differences in the timing, location, and magnitude of the responses. In particular, the model responses are in general stronger than the observed responses. While these differences may be in part attributed to potential differences in the timing and locations of the modeled and observed aerosol, the aerosol properties in the WACCM SAD data set have been validated extensively in Mills et al. (2016) and Schmidt et al. (2018). Among other factors that could affect correlations found in observations versus the model are model errors in chemistry, noise in the observations, and interference between the aerosols and the chemical signals needed for the satellite retrievals. Changes in solar irradiance were not included in the model simulations; such changes can affect the dynamics (Kodera & Kuroda, 2002) and chemistry (Matthes et al., 2010; Shindell et al., 1999) of the stratosphere, though the difference in, for example, ozone abundance was found to be less than 5% between solar maxima and minima. In addition, a 28-month, cyclic QBO was imposed in the WACCM ensemble. The repeated 28-month cycle does not capture the full variability of the QBO, including potential aerosol effects on the QBO. In this way, simplifications in the model setup certainly play a role in the more consistent chemical response in the model. However, tests suggest that the time intervals considered may be the most important driver of the differences and are constrained by data availability. The 2005–2014 period for analysis of observations was

used purely because of the availability of MLS measurements, while 1999–2013 was used for WACCM because years outside this interval were forced with repeating year 2000 aerosol loading in these simulations. Relative to the 1999–2004 period, 2005–2013 was much more volcanically active. In terms of sulfur dioxide (SO_2) loading, the eruptions in Table S1 spanning 1999–2004 account for an average of 0.06 Tg SO_2/year, while the average for the eruptions over 2005–2013 is 0.8 Tg SO_2/year. We demonstrate the impact that the choice of base period and background concentrations has on the response in Figures S15–S18, where we use the same period as in the observations (2005–2013) to compute the WACCM anomalies. This has a very large effect on the results. Figures S15–S17 show that NO_y/Cl_y-SAD correlations are about 20% lower in magnitude when excluding 1999–2004. This is further illustrated in the WACCM SAD correlation coefficients in Figures S18a–S18c, which are reduced by up to half when considering only 2005–2013, and then show much better agreement with the observations (Figures S18d–S18f) in terms of magnitudes of the correlations.

Park et al. (2017), among others, showed the strong dependence of variability of stratospheric trace gases and the QBO, as well as the compact relationship between N_2O and NO_y; we have shown that the latter can be exploited to remove anomalies related to dynamical variability, the most prevalent form of which is the QBO (e.g., Randel & Wu, 1996). Application of the N_2O regression in conjunction with a traditional QBO regression has been shown to be a more effective method for removing a majority of transport-related anomalies than either one alone, which is essential for isolating the chemical response to volcanic aerosol.

6. Conclusions

In this study, we sought to probe the stratospheric NOy/Cly response to recent increases in stratospheric volcanic aerosol concentrations. Related to the occurrence of a series of moderate-magnitude volcanic eruptions between 2005 and 2014, we found a clear response in stratospheric NO_y concentrations in both the WACCM ensemble and the observations, with some distinct differences. While OSIRIS NO_x shows decreases during times of increased volcanic aerosol concentrations at and below 10 hPa, the response is much more consistent in WACCM, with respect to both the mean and individual ensemble members; this is evident in the much higher correlation coefficients for WACCM NO_x. In general, WACCM appears to simulate the chemical response much more consistently. When hydrolysis of N_2O_5 increases, depleting the NO_x reservoir, HNO_3, is enhanced. This response is also seen in the WACCM ensemble and MLS observations, though there are some differences in the timing and location as compared to the NO_x response. In particular, HNO_3 enhancements are more prevalent at higher altitudes than NO_x reductions. In addition, compared to lower altitudes, some of the largest perturbations from the mean in the WACCM SAD data set at ~20–5 hPa occur before 2005; this undoubtedly has an impact on the somewhat reduced response in MLS HNO_3 for which the observations begin in 2005. For ClO, WACCM simulates robust increases at and below 20 hPa as a result of the NO_x depletion. Similar ClO enhancements are absent from the MLS observations but are likely below the detection threshold for the instrument.

In summary, our results demonstrate that recent moderate volcanic eruptions have affected NO_x, HNO_3, and ClO concentrations in the stratosphere. The use of N_2O data along with QBO winds as a means of accounting for dynamical and chemical variability has also been shown to allow improved identification of such chemical signatures as distinct from dynamical noise. Finally, ensemble simulations are an important tool in ensuring a robust understanding of the SNR ratios of such responses and hence interpreting the single realization available in observations. The results presented here further highlight the impact of moderate volcanic activity, can help to improve predictability following a future volcanic eruption, and underline the importance and utility of N_2O observations for distinguishing the effects of heterogeneous chemistry from natural variability on stratospheric composition.

References

Adams, C., Bourassa, A. E., McLinden, C. A., Sioris, C. E., von Clarmann, T., Funke, B., et al. (2017). Effect of volcanic aerosol on stratospheric NO_2 and N_2O_5 from 2002–2014 as measured by Odin-OSIRIS and Envisat-MIPAS. *Atmospheric Chemistry and Physics*, *17*(13), 8063–8080. https://doi.org/10.5194/acp-17-8063-2017

Avallone, L. M., Toohey, D. W., Proffitt, M. H., Margitan, J. J., Chan, K. R., & Anderson, J. G. (1993). In situ measurements of ClO at mid-latitudes: Is there an effect from Mt. Pinatubo? *Geophysical Research Letters*, *20*(22), 2519–2522. https://doi.org/10.1029/93GL02418

Berthet, G., Jégou, F., Catoire, V., Krysztofiak, G., Renard, J. B., Bourassa, A. E., et al. (2017). Impact of a moderate volcanic eruption on chemistry in the lower stratosphere: Balloon-borne observations and model calculations. *Atmospheric Chemistry and Physics*, *17*(3), 2229–2253. https://doi.org/10.5194/acp-17-2229-2017

Bittner, M., Timmreck, C., Schmidt, H., Toohey, M., & Krüger, K. (2016). The impact of wave-mean flow interaction on the Northern Hemisphere polar vortex after tropical volcanic eruptions. *Journal of Geophysical Research: Atmospheres*, *121*, 5281–5297. https://doi.org/10.1002/2015JD024603

Bourassa, A. E., Degenstein, D. A., Randel, W. J., Zawodny, J. M., Kyrölä, E., McLinden, C. A., et al. (2014). Trends in stratospheric ozone derived from merged SAGE II and Odin-OSIRIS satellite observations. *Atmospheric Chemistry and Physics*, *14*(13), 6983–6994. https://doi.org/10.5194/acp-14-6983-2014

Bourassa, A. E., McLinden, C. A., Sioris, C. E., Brohede, S., Bathgate, A. F., Llewellyn, E. J., & Degenstein, D. A. (2011). Fast NO_2 retrievals from Odin-OSIRIS limb scatter measurements. *Atmospheric Measurement Techniques*, *4*(5), 965–972. https://doi.org/10.5194/amt-4-965-2011

Brasseur, G. P., & Solomon, S. (2005). *Aeronomy of the middle atmosphere*, (p. 646). Netherlands: Springer. https://doi.org/10.1007/1-4020-3824-0

Coffey, M. T. (1996). Observations of the impact of volcanic activity on stratospheric chemistry. *Journal of Geophysical Research*, *101*(D3), 6767–6780. https://doi.org/10.1029/95JD03763

Dee, D. P., Uppala, S. M., Simmons, A. J., Berrisford, P., Poli, P., Kobayashi, S., et al. (2011). The ERA-Interim reanalysis: Configuration and performance of the data assimilation system. *Quarterly Journal of the Royal Meteorological Society*, *137*(656), 553–597. https://doi.org/10.1002/qj.828

Deser, C., Philips, A. S., Alexander, M. A., & Smoliak, B. V. (2014). Projecting North American climate over the next 50 years: Uncertainty due to internal variability. *Journal of Climate*, *27*(6), 2271–2296. https://doi.org/10.1175/JCLI-D-13-00451.1

Eyring, V., Lamarque, J. F., Hess, P., Arfeuille, F., Bowman, K., Chipperfiel, M. P., et al. (2013). Overview of IGAC/SPARC Chemistry-Climate Model Initiative (CCMI) community simulations in support of upcoming ozone and climate assessments. *SPARC Newsletter*, *40*, 48–66.

Fujino, J., Nair, R., Kainuma, M., Masui, T., & Matsuoka, Y. (2006). Multi-gas mitigation analysis on stabilization scenarios using AIM global model. *The Energy Journal*, *27*(SI3). https://doi.org/10.5547/ISSN0195-6574-EJ-VolSI2006-NoSI3-17

Garcia, R. R., Smith, A. K., Kinnison, D. E., de la Camara, A., & Murphy, D. (2017). Modification of the gravity wave parameterization in the Whole Atmosphere Community Climate Model: Motivation and results. *Journal of the Atmospheric Sciences*, *74*(1), 275–291. https://doi.org/10.1175/JAS-D-16-0104.1

Hanson, D. R., Ravishankara, A. R., & Solomon, S. (1994). Heterogeneous reactions in sulfuric acid aerosols: A framework for model calculations. *Journal of Geophysical Research*, *99*(D2), 3615–3629. https://doi.org/10.1029/93JD02932

Hijioka, Y., Matsuoka, Y., Nishimoto, H., Masui, M., & Kainuma, M. (2008). Global GHG emissions scenarios under GHG concentration stabilization targets. *Journal of Global Environment Engineering*, *13*, 97–108.

Hurrell, J. W., Holland, M. M., Gent, P. R., Ghan, S., Kay, J. E., Kushner, P. J., et al. (2013). The Community Earth System Model: A framework for collaborative research. *Bulletin of the American Meteorological Society*, *94*(9), 1339–1360. https://doi.org/10.1175/BAMS-D-12-00121.1

Johnston, P. V., McKenzie, R. L., Keys, J. G., & Matthews, W. A. (1992). Observations of depleted stratospheric NO_2 following the Pinatubo volcanic eruption. *Geophysical Research Letters*, *19*(2), 211–213. https://doi.org/10.1029/92GL00043

Kay, J. E., Deser, C., Phillips, A., Mai, A., Hannay, C., Strand, G., et al. (2015). The Community Earth System Model (CESM) large ensemble project: A community resource for studying climate change in the presence of internal climate variability. *Bulletin of the American Meteorological Society*, *96*(8), 1333–1349. https://doi.org/10.1175/BAMS-D-13-00255.1

Kinnison, D. E., Brasseur, G. P., Walters, S., Garcia, R. R., Marsh, D. R., Sassi, F., et al. (2007). Sensitivity of chemical tracers to meteorological parameters in the MOZART3 chemical transport model. *Journal of Geophysical Research*, *112*, D20302. https://doi.org/10.1029/2006JD007879

Kodera, K., & Kuroda, Y. (2002). Dynamical response to the solar cycle. *Journal of Geophysical Research*, *107*(D24), 4749. https://doi.org/10.1029/2002JD002224

Lambert, A., Read, W. G., Livesey, N. J., Santee, M. L., Manney, G. L., Froidevaux, L., et al. (2007). Validation of the Aura Microwave Limb Sounder middle atmosphere water vapor and nitrous oxide measurements. *Journal of Geophysical Research*, *112*, D24S36. https://doi.org/10.1029/2007JD008724

Livesey, N. J., Read, W. G., Froidevaux, L., Lambert, A., Manney, G. L., Pumphrey, H. C., et al. (2013). *Earth Observing Sattelite (EOS) Aura Microwave Limb Sounder (MLS) version 3.3 and 3.4 Level 2 data quality and description document (Technical Report JPL D-33509)*. Pasadena, CA: Jet Propulsion Laboratory. http://mls.jpl.nasa.gov/

Livesey, N. J., Read, W. G., Wagner, P. A., Froidevaux, L., Lambert, A., Manney, G. L., et al. (2017). *Earth Observing System (EOS) Aura Microwave Limb Sounder (MLS) version 4.2x Level 2 data quality and description document (Technical Report JPL D-33509 Rev. D)*. Pasadena, CA: Jet Propulsion Laboratory. http://mls.jpl.nasa.gov/

Llewellyn, E. J., Lloyd, N. D., Degenstein, D. A., Gattinger, R. L., Petelina, S. V., Bourassa, A. E., et al. (2004). The OSIRIS instrument on the Odin satellite. *Canadian Journal of Physics*, *82*(6), 411–422. https://doi.org/10.1139/P04-005

Marsh, D. R., Mills, M. J., Kinnison, D. E., Lamarque, J. F., Calvo, N., & Polvani, L. M. (2013). Climate change from 1850 to 2005 simulated in CESM1(WACCM). *Journal of Climate*, *26*(19), 7372–7391. https://doi.org/10.1175/JCLI-D-12-00558.1

Matthes, K., Marsh, D. R., Garcia, R. R., Kinnison, D. E., Sassi, F., & Walters, S. (2010). Role of the QBO in modulating the influence of the 11 year solar cycle on the atmosphere using constant forcings. *Journal of Geophysical Research*, *115*, D18110. https://doi.org/10.1029/2009JD013020

McLinden, C. A., Bourassa, A. E., Brohede, S., Cooper, M., Degenstein, D. A., Evans, W. J. F., et al. (2012). OSIRIS: A decade of scattered light. *Bulletin of the American Meteorological Society*, *93*(12), 1845–1863. https://doi.org/10.1175/BAMS-D-11-00135.1

McLinden, C. A., Olsen, S. C., Hannegan, B., Wild, O., Prather, M. J., & Sundet, J. (2000). Stratospheric ozone in 3-D models: A simple chemistry and the cross-tropopause flux. *Journal of Geophysical Research*, *105*(D11), 14,653–14,665. https://doi.org/10.1029/2000JD900124

Mickley, L. J., Abbatt, J. P. D., Frederick, J. E., & Russell, J. M. III (1997). Response of summertime odd nitrogen and ozone at 17 mbar to Mount Pinatubo aerosol over the southern midlatitudes: Observations from the Halogen Occultation Experiment. *Journal of Geophysical Research*, *102*(D19), 23,573–23,582. https://doi.org/10.1029/97JD01566

Mills, M. J., Langford, A. O., O'Leary, T. J., Arpag, K., Miller, H. L., Proffitt, M. H., & Solomon, S. (1993). On the relationship between stratospheric aerosols and nitrogen dioxide. *Geophysical Research Letters*, *20*(12), 1187–1190. https://doi.org/10.1029/93GL01124

Mills, M. J., Schmidt, A., Easter, R., Solomon, S., Kinnison, D. E., Ghan, S. J., et al. (2016). Global volcanic aerosol properties derived from emissions, 1990–2014, using CESM1(WACCM). *Journal of Geophysical Research: Atmospheres*, *121*, 2332–2348. https://doi.org/10.1002/2015JD024290

Mote, P. W., Rosenlof, K. H., McIntyre, M. E., Carr, E. S., Gille, J. C., Holton, J. R., et al. (1996). An atmospheric tape recorder: The imprint of tropical tropopause temperatures on stratospheric water vapor. *Journal of Geophysical Research*, *101*(D2), 3989–4006. https://doi.org/10.1029/95JD03422

Naujokat, B. (1986). An update of the observed quasi-biennial oscillation of the stratospheric winds over the tropics. *Journal of the Atmospheric Sciences*, *43*(17), 1873–1877. https://doi.org/10.1175/1520-0469(1986)043<1873:AUOTOQ>2.0.CO;2

Neely III, R.R. and Schmidt, A. (2016). VolcanEESM: Global volcanic sulphur dioxide (SO2) emissions database from 1850 to present—Version 1.0. Centre for Environmental Data Analysis, 04 February 2016. https://doi.org/10.5285/76ebdc0b-0eed-4f70-b89e-55e606bcd568

Otto-Bliesner, B. L., Brady, E. C., Fasullo, J., Jahn, A., Landrum, L., Stevenson, S., et al. (2016). Climate variability and change since 850 CE: An ensemble approach with the Community Earth System Model. *Bulletin of the American Meteorological Society*, *97*(5), 735–754. https://doi.org/10.1175/BAMS-D-14-00233.1

Park, M., Randel, W. J., Kinnison, D. E., Bourassa, A. E., Degenstein, D. A., Roth, C. Z., et al. (2017). Variability of stratospheric reactive Nitrogen and Ozone related to the QBO. *Journal of Geophysical Research: Atmospheres*, *122*, 10,103–10,118. https://doi.org/10.1002/2017JD027061

Prather, M. (1992). Catastrophic loss of stratospheric ozone in dense volcanic clouds. *Journal of Geophysical Research*, *97*(D9), 10,187–10,191. https://doi.org/10.1029/92JD00845

Randel, W. J., & Thompson, A. M. (2011). Interannual variability and trends in tropical ozone derived from SAGE II satellite data and SHADOZ ozonesondes. *Journal of Geophysical Research*, *116*, D07303. https://doi.org/10.1029/2010JD015195

Randel, W. J., & Wu, F. (1996). Isolation of the ozone QBO in SAGE II data by singular-value decomposition. *Journal of the Atmospheric Sciences*, *53*(17), 2546–2559. https://doi.org/10.1175/1520-0469(1996)053<2546:IOTOQI>2.0.CO;2

Rienecker, M. M., Suarez, M. J., Gelaro, R., Todling, R., Bacmeister, J., Liu, E., et al. (2011). MERRA: NASA's Modern-Era Retrospective Analysis for Research and Applications. *Journal of Climate*, *24*(14), 3624–3648. https://doi.org/10.1175/JCLI-D-11-00015.1

Rinsland, C. P., Chiou, L., Boone, C., Bernath, P., Mahieu, E., & Zander, R. (2009). Trend of lower stratospheric methane (CH_4) from atmospheric chemistry experiment (ACE) and atmospheric trace molecule spectroscopy (ATMOS) measurements. *Journal of Quantitative Spectroscopy and Radiation Transfer*, *110*(13), 1066–1071. https://doi.org/10.1016/j.jqsrt.2009.03.024

Rinsland, C. P., Gunson, M. R., Abrams, M. C., Lowes, L. L., Zander, R., Mahieu, E., et al. (1994). Heterogeneous conversion of N_2O_5 to HNO_3 in the post-Mount Pinatubo eruption stratosphere. *Journal of Geophysical Research*, *99*(D4), 8213–8219. https://doi.org/10.1029/93JD03469

Santee, M. L., Lambert, A., Read, W. G., Livesey, N. J., Cofield, R. E., Cuddy, D. T., et al. (2007). Validation of the Aura Microwave Limb Sounder HNO_3 measurements. *Journal of Geophysical Research*, *112*, D24S60. https://doi.org/10.1029/2007JD008721

Santee, M. L., Lambert, A., Read, W. G., Livesey, N. J., Manney, G. L., Cofield, R. E., et al. (2008). Validation of the Aura Microwave Limb Sounder ClO measurements. *Journal of Geophysical Research*, *113*(D15), D15S22. https://doi.org/10.1029/2007JD008762

Schmidt, A., Mills, M. J., Ghan, S., Gregory, J. M., Allan, R. P., Andrews, T., et al. (2018). Volcanic radiative forcing from 1979 to 2015. *Journal of Geophysical Research: Atmospheres*, *123*, 12–508. https://doi.org/10.1029/2018JD028776

Shindell, D., Rind, D., Balachandran, N., Lean, J., & Lonergan, P. (1999). Solar cycle variability, ozone, and climate. *Science*, *284*(5412), 305–308. https://doi.org/10.1126/science.284.5412.305

Sioris, C. E., Haley, C. S., McLinden, C. A., von Savigny, C., McDade, I. C., McConnell, J. C., et al. (2003). Stratospheric profiles of nitrogen dioxide observed by Optical Spectrograph and Infrared Imager System on the Odin satellite. *Journal of Geophysical Research*, *108*(D7), 4215. https://doi.org/10.1029/2002JD002672

Sioris, C. E., Kurosu, T. P., Martin, R. V., & Chance, K. (2004). Stratospheric and tropospheric NO_2 observed by SCIAMACHY: First results. *Advances in Space Research*, *34*(4), 780–785. https://doi.org/10.1016/j.asr.2003.08.066

Sioris, C. E., McLinden, C. A., Martin, R. V., Sauvage, B., Haley, C. S., Lloyd, N. D., et al. (2007). Vertical profiles of lightning-produced NO_2 enhancements in the upper troposphere observed by OSIRIS. *Atmospheric Chemistry and Physics*, *7*(16), 4281–4294. https://doi.org/10.5194/acp-7-4281-2007

Sioris, C. E., Rieger, L. A., Lloyd, N. D., Bourassa, A. E., Roth, C. Z., Degenstein, D. A., et al. (2017). Improved OSIRIS NO_2 retrieval algorithm: Description and validation. *Atmospheric Measurement Techniques*, *10*(3), 1155–1168. https://doi.org/10.5194/amt-10-1155-2017

Solomon, S., Daniel, J. S., Neely, R. R. III, Vernier, J. P., Dutton, E. G., & Thomason, L. W. (2011). The persistently variable "background" stratospheric aerosol layer and global climate change. *Science*, *333*(6044), 866–870. https://doi.org/10.1126/science.1206027

Solomon, S., Kinnison, D. E., Bandoro, J., & Garcia, R. (2015). Simulations of polar ozone depletion: An update. *Journal of Geophysical Research: Atmospheres*, *120*, 7958–7974. https://doi.org/10.1002/2015JD023365

Stolarski, R. S., Douglass, A. R., & Strahan, S. E. (2018). Using satellite measurements of N_2O to remove dynamical variability from HCl measurements. *Atmospheric Chemistry and Physics*, *18*(8), 5691–5697. https://doi.org/10.5194/acp-18-5691-2018

Thomason, L. W., Ernest, N., Millán, L., Rieger, L., Bourassa, A., Vernier, J. P., et al. (2018). A global space-based stratospheric aerosol climatology: 1979–2016. *Earth System Science Data Data*, *10*(1), 469–492. https://doi.org/10.5194/essd-10-469-2018

Tilmes, S., Lamarque, J. F., Emmons, L. K., Kinnison, D. E., Marsh, D., Garcia, R. R., et al. (2016). Representation of the Community Earth System Model (CESM1) CAM4-Chem within the Chemistry-Climate Model Initiative. *Geoscientific Model Development*, *9*(5), 1853–1890. https://doi.org/10.5194/gmd-9-1853-2016

Waters, J. W., Froidevaux, L., Harwood, R. S., Jarnot, R. F., Pickett, H. M., Read, W. G., et al. (2006). The Earth Observing System Microwave Limb Sounder (EOS MLS) on the Aura satellite. *IEEE Transactions on Geoscience and Remote Sensing*, *44*(5), 1075–1092. https://doi.org/10.1109/TGRS.2006.873771

Wegner, T., Grooß, J.-U., von Hobe, M., Stroh, F., Sumińska-Ebersoldt, O., Volk, C. M, et al. (2012). Heterogeneous chlorine activation on stratospheric aerosols and clouds in the Arctic polar vortex. *Atmospheric Chemistry and Physics*, *12*(22), 11,095–11,106. https://doi.org/10.5194/acp-12-11095-2012